Applied Catalysis B: Environmental 303 (2022) 120881

Contents lists available at ScienceDirect

Applied Catalysis B: Environmental

journal homepage: www.elsevier.com/locate/apcatb

Realizing a redox-robust Ag/MnO_2 catalyst for efficient wet catalytic ozonation of S-VOCs: Promotional role of Ag(0)/Ag(I)-Mn based redox shuttle

Chun He [a], Yuhong Liao [a], Cheng Chen [a], Dehua Xia [a,*], Yongyi Wang [a], Shuanghong Tian [a], Jingling Yang [b,*], Dong Shu [c]

[a] Guangdong Provincial Key Laboratory of Environmental Pollution Control and Remediation Technology, School of Environmental Science and Engineering, Sun Yat-sen University, Guangzhou 510275, China
[b] School of Environment, Jinan University, Guangzhou 510632, China
[c] Key Lab of Technology on Electrochemical Energy Storage and Power Generation in Guangdong Universities, School of Chemistry and Environment, South China Normal University, Guangzhou 510006, China

ARTICLE INFO

Keywords:
Wet catalytic ozonation
S-VOCs
Strong metal-metal oxide interaction
Heterogeneous catalysis

ABSTRACT

A novel process for S-VOCs degradation using wet scrubbing coupled with catalytic ozonation was developed for first time. We report redox-robust catalysts consisting of Ag(0)/Ag(I) species decorated rambutan-like MnO_2 hollow microspheres (Ag/R-MnO_2) with strong metal-metal oxide interaction (MMOI) exhibited superior catalytic ozonation performance for CH_3SH elimination. The optimum Ag/R-MnO_2 reached a significant improvement in CH_3SH elimination of 96.9% conversion over pristine R-MnO_2 under GHSV of 75,000 mL h^{-1} g^{-1}, and O_3 utilization rate of 92.3%. An outstanding stability of Ag/R-MnO_2 under wet catalytic ozonation process was demonstrated, which outperformed that in gaseous system. CH_3SH was captured by aqueous solution and preferentially chemisorbed on Ag, then deeply oxidized to the final products of SO_4^{2-}/CO_3^{2-} via catalytic ozonation by multivalent R-MnO_2. The excellent performance can be ascribed to efficient electron replenishing interaction between Ag(0)/Ag(I) and multivalent R-MnO_2, efficient O_3 activation through oxygen vacancies-rich R-MnO_2, and enhanced mass diffusion in wet scrubbing process.

1. Introduction

Recently, odorous pollution has gained increasing public concern due to their detrimental impact on the environment and human health. Especially, sulfur-containing volatile organic compounds (S-VOCs) were believed to be one of the most important contributors to odorous pollution [1]. Methyl mercaptan (CH_3SH) which mainly derived from petroleum refining, wood pulping and sewage treatment is a representative S-VOCs with an olfactory threshold of around 0.4 ppb/v, and the exposure of CH_3SH can cause severe damage to the respiratory and nervous system of human beings [2–4]. A variety of purification techniques have been explored for odor elimination, such as biological process, adsorption, catalytic combustion technology. However, the widespread application of them is held back by their high cost, large energy input and low efficiency [5–7]. As an alternative, ozonation has been considered as one of the most promising methods for S-VOCs treatment owing to its advantages of that easy implementation, high efficiency and low energy input [8].

Although ozone is an efficient oxidant, ozonation alone is inadequate for the entire degrading organic pollutants due to its selectivity [9]. Significantly, ozonation in the presence of a catalyst promotes the activation of ozone to more reactive states for deeply decomposition of contaminants. It has been a vital task to seek an active and stable ozonation catalyst in recent years [10]. By far, manganese oxide is the most widely studied metal oxide as an ozonation catalyst because of its unique characteristics, such as environmental friendliness, plentiful valence states, facile fabrication, and low cost [11,12]. However, most of the ozonation catalysts still suffer from incomplete decomposition of contaminants, poor ozone utilization and severe instability which limit the widespread application of catalytic ozonation technology. Therefore, the development of efficient and robust ozonation catalysts grows to be of great importance. The critical factors which constrain the

* Correspondence to: School of Environmental Science and Engineering, Sun Yat-sen University, Guangzhou 510275, China.
E-mail addresses: xiadehua3@mail.sysu.edu.cn (D. Xia), yangjl@jnu.edu.cn (J. Yang).

https://doi.org/10.1016/j.apcatb.2021.120881
Received 22 October 2020; Received in revised form 18 October 2021; Accepted 28 October 2021
Available online 31 October 2021

performance of ozonation catalysts including poor electron replenishment and easy deactivation by adsorbed reactants and intermediate products during the catalytic ozonation [13,14]. Constructing novel catalytic ozonation systems to ensure dynamically replenish electrons and efficient mass transfer is expected to make a breakthrough for those technological difficulties.

Metal/metal oxide composites with strong metal-metal oxide interaction (MMOI) has been reported to possess significant catalytic activity and durability [15]. MMOI between the noble metal and the metal oxide support are known to give rise to electronic, geometric and bifunctional effect, which facilitates the oxygen migration, promotes the electron replenishing, and provides dual active sites at the perimeter between the metal and the metal oxide leading to significantly improved catalytic activity as well. Yang et al. reported the strong MMOI between Pt nanoparticles and $SrTiO_3$ facilitated the generation and transfer of photo-excited hot electrons (from Pt to $SrTiO_3$), resulting in the enhanced oxygen activation and photothermocatalytic oxidation of toluene [16]. Moreover, Li et al. reported the MMOI effect of Ag@Pd NPs/MnO_2 can facilitate the lattice oxygen migration from MnO_2 to palladium, resulting in the state phase transformation from Pd^0 to PdO_2, and the oxidation state of manganese in the MnO_2 is changed from Mn (IV) to Mn(III) simultaneously [17]. Thus, more active sites were exposed for VOCs purification. Therefore, it is expected to significantly enhance the catalytic ozonation of CH_3SH by constructing MMOI in ozonation catalysts to promote dynamical electron replenishment.

At the same time, the deactivation of catalysts during the catalytic removal of S-VOCs has also been regarded as a critical issue restricting the catalytic performance. The main mechanism for the deactivation of S-VOCs stream was the poisoning by sulfur species that adsorbed on the active sites of catalysts, which blocked the access of reactants to catalyst [7,18]. As mentioned above, the deactivation of catalyst can be delayed or prevented by enhancing the surface diffusion of poisoning species. The wet scrubbing process has been demonstrated as a promising approach to migrate out the formed intermediates and products from the heterogenous catalyst, avoiding their accumulation on surface [19]. Inspired by this, the coupling process of catalytic oxidation and wet scrubbing has been developed to overcome the catalysts deactivation. Compare with the commonly used gaseous phase catalytic system, the reported wet catalytic system could facilitate the capture of water-soluble pollutants, thus, improving the activity and stability. Recently, there are some reports on the efficient degradation of gaseous VOCs by this new coupling process [20–22]. To the best of our knowledge, yet no study has been reported on the wet scrubbing coupled with catalytic ozonation for CH_3SH removal.

Given that MMOI in metal/metal oxide catalyst has been reported that it can promote the catalytic reactions [23], and wet scrubbing is a promising approach to avoid the catalysts deactivation [24]. In this work, we specially designed a redox-stabilized Ag/rambutan-like MnO_2 hollow microspheres (Ag/R-MnO_2) with MMOI effect for catalytic ozonation of CH_3SH in a wet scrubbing reactor under mild condition. The MMOI in Ag/R-MnO_2 was constructed through MnO_2-site-directed photoreduction of Ag(I) to Ag(0). The removal rate of CH_3SH and the utilization rate of O_3 by Ag/R-MnO_2 at room temperature were investigated. Especially, the long-term catalytic performance of Ag/R-MnO_2 in wet catalytic ozonation is compared with that in gas phase system. Secondly, the relationships between properties and catalytic activity for S-VOCs oxidation and O_3 decomposition through redox-robust Ag/R-MnO_2 were unraveled via a variety of characterization techniques including XRD, SEM, TEM, Raman, H_2-TPR, O_2-TPR, in situ DRIFT and XPS. The electron replenishes dynamically between Ag (0)/Ag(I) and Mn(II)/Mn(III)/Mn(IV) and the efficient activation of O_3 through the oxygen vacancies in R-MnO_2, as well as the enhanced mass diffusion in wet scrubbing process ensuring the outstanding catalytic performance. Finally, a possible degradation pathway in this coupling process was proposed based on the evolution of intermediates and products from CH_3SH degradation.

2. Experimental section

2.1. Preparation of catalysts

2.1.1. Preparation of R-MnO_2

3D rambutan-like MnO_2 hollow microspheres were successfully synthesized via a hydrothermal method [25]. 0.01 mol $MnSO_4$ and 0.015 mol $KClO_3$ were added to concentrated nitric acid (68%) in a conical flask under constant stirring for 20 min in a water bath at 80 ℃. Subsequently, the resulting suspension was transferred into a Teflon-lined stainless-steel autoclave and maintained at 120 ℃ for 6 h. The obtained product was collected by filtration, washed with ultrapure deionized water, and then dried at 60 ℃. The obtained powder was identified as 3D rambutan-like MnO_2 hollow microspheres and correspondingly labeled as R-MnO_2.

2.1.2. Preparation of Ag/R-MnO_2

Ag/R-MnO_2 was prepared via a photoreduction method. 0.5 g of the as-prepared R-MnO_2 was dispersed in 100 mL of 0.2 mmol/L $AgNO_3$ solution, and irradiated under a Xenon lamp under stirring for 30 min [26]. The precipitate was separated, washed, and dried in vacuum overnight, and labeled as 2.58% Ag/R-MnO_2. In comparison, the addition amount of $AgNO_3$ was adjusted from 0.02 to 10.0 mmol/L, and the obtained products were correspondingly labeled as 0.26% Ag/R-MnO_2, 5.63% Ag/R-MnO_2 and 6.83% Ag/R-MnO_2, respectively.

2.2. Characterization of catalysts

X-ray diffraction (XRD) measurement was determined on Rigaku D/MAX 2500 X-ray diffractometer equipped with Cu Kα radiation source at 40 kV and 30 mA. The morphologies of catalysts were observed using a Quanta 400 FEG thermal field emission scanning electron microscopy (SEM) with an X-ray dispersive energy (EDS) analyzer. Transmission emission microscopy (TEM) images and element mapping results were taken on a JEM-2100F (JOEL, Japan) with an accelerating voltage of 200 kV. Raman spectra were performed through a Renishaw inVia Laser Micro-Raman Spectrometer with an excitation source of 514.5 nm. X-ray photoelectron spectroscopy (XPS) spectra were determined on a Nexsa XPS System (Thermo Fisher, USA). Fourier transform infrared (FTIR) spectroscopy was carried out using a Nicolet iS10 FTIR spectrometer (Thermo Scientific, USA) with 10 mg of fresh catalyst or used catalyst placed in a Harrick Scientific Praying Mantis cell. H_2 temperature-programmed reduction (H_2-TPR) and O_2 temperature-programmed desorption (O_2-TPD) were performed on an AutoChem II 2920 Chemisorption Analyzer (Micromeritics, USA). Reactive oxygen species (ROS) were measured by electron spin-resonance resonance (ESR) experiments using a A300 spectrometer (Bruker, Germany). Hydroxyl radicals (•OH) and superoxide radicals ($\bullet O_2^-$) were trapped with 5,5-dimethyl-1-pyrroline-N-oxide (DMPO), and singlet oxygen ($^1O_2$) were trapped with 2,2,6,6-tetramethylpiperidine (TEMP). A fluorescence spectrophotometer (Thermo Scientific Lumina, USA) was used to obtain Fluorescence spectra of 2-hydroxyterephthalic at an excitation wavelength of 315 nm. 0.5 mol/L terephthalic acid dissolved in 1 mmol/L NaOH solution was used as a fluorescent probe. *In-situ* ATR-FTIR spectra were recorded by a HATR Flow-Through Cell. The cell was mounted on an attachment for the measurements by a Nicolet iS10 FTIR spectrometer. The spectra were scanned in the range of 4000–800 cm^{-1} with a resolution of 4 cm^{-1} and averaging 32 scans. The sulfur-containing ionic products were quantified by a Metrohm 882 Compact ion chromatography (IC).

2.3. Experimental setup

The catalytic ozonation process was carried out in a continuous flow mode. In the wet catalytic ozonation of CH_3SH, 120 mg catalysts were dispersed in a magnetically stirred cylindrical quartz reactor with a size of 50 mm in diameter and 350 mm in height. The liquid volume was 600

mL. The initial pH of solution was adjusted using 0.1 mol/L HCl and 0.1 mol/L NaOH, and measured by pH meter. The inlet CH_3SH was diluted with nitrogen, and then fed to the bottom of the column reactor continuously through a corundum aerator. The total flow rate was kept at 150 mL min^{-1}. The inlet concentration of CH_3SH was controlled at about 75 ppm, and the outlet concentration of CH_3SH was measured by a CH_3SH sensor (DM-400IS, Detcon, USA). Ozone was produced by an ozone generator (YE-TG-02P, YDG, China) using pure oxygen as the intake. The inlet ozone concentration was kept at 30 ppm, and the outlet concentration of ozone was measured by an ozone analyzer (106-M, 2B technologies, USA). As a contrast, the catalytic ozonation of CH_3SH in gaseous system was conducted in a column reactor with diameter of 30 mm, and other experimental parameters were identical with those in wet scrubbing system.

3. Results and discussion

3.1. Characterization of catalysts

The synthesis process of Ag/rambutan-like MnO_2 (Ag/R-MnO_2) catalyst is schematically illustrated in Fig. 1a. The R-MnO_2 hollow microspheres were synthesized through a facile hydrothermal method, and the influence of hydrothermal time on activity of MnO_2 is shown in Text S1 and Figs. S1–S3. Then, Ag species were deposited on the R-MnO_2 via MnO_2-site-directed reduction upon light irradiation. The commonly used reduction methods, such as thermal methods, chemical methods that introduce hydrogen or $NaBH_4$ are somewhat unsatisfactory due to the high energy waste with respect to the residual contamination derived from chemical reducing agents or high temperature treatment. Recently, photoreduction has emerged as an appealing alternative for commonly used reduction methods (e.g. thermal methods, chemical methods that introduce hydrogen or $NaBH_4$), because photoreduction does not rely on either toxic chemicals or high temperature [27,28].

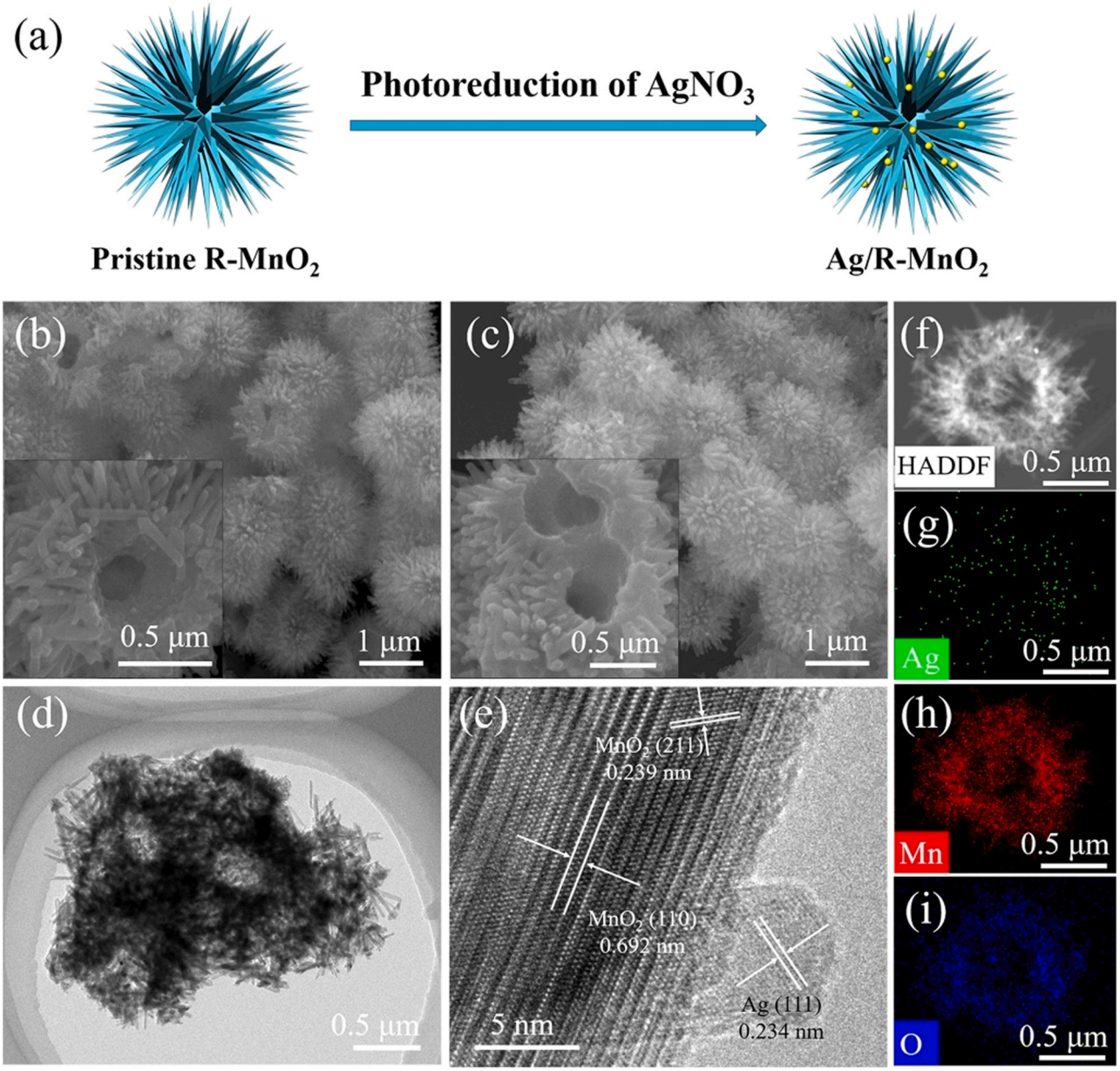

Fig. 1. (a) Schematic of synthetic process for Ag/R-MnO_2; SEM images of (b)R-MnO_2 and (c) 2.58% Ag/R-MnO_2; (d) TEM image, (e) HRTEM image and (f–i) Cs-corrected HAADF-STEM with element mapping images of 2.58% Ag/R-MnO_2.

Moreover, it has been reported that the photo-reduction process can provide the ideal condition for the formation of strong interaction between metal and metal oxide [29]. As shown in Fig. 1b, the pristine MnO_2 demonstrates a rambutan-like hollow spherical structure with rich needle-like cutting-edges that facilitate the dispersion of Ag species. Besides, the dedicate rambutan-like structure with well-defined interior voids is able to capture gaseous reactants, prolong the retention time of reactants[10]. According to the SEM images shown in Fig. 1c, no significant morphology change can be observed on 2.58% Ag/R-MnO_2 after Ag deposition, indicating that the deposition of Ag has not deteriorated the morphology of R-MnO_2. The morphology of samples with different Ag proportions is shown in Fig. S4, and the amount of Ag was determined by EDS characterization (Table S1). Moreover, TEM image also verifies the 3D hollow structure of 2.58% Ag/R-MnO_2 (Fig. 1d). The HRTEM image shown in Fig. 1e demonstrates the intimate contact between the nanoparticle and the nanorod, in which the nanoparticle with a size of about 8 nm and interplanar spacing of 0.234 nm, corresponding to the spacing of the (111) plane of Ag, and the lattice spacing of 0.239 and 0.692 nm on the nanorod can be assigned to the (211) and (110) plane of MnO_2. The precise elemental mappings of in Fig. 1f-i reveal that Mn, O and Ag elements are homogeneously dispersed in the entire rambutan-like nanostructure, confirmed the uniform deposition of Ag species on R-MnO_2. The N_2 adsorption-desorption isotherms of R-MnO_2 and Ag/R-MnO_2 are shown in Fig. S5. The S_{BET} surface area of R-MnO_2 and Ag/R-MnO_2 is 156.5 and 154.1 $m^2\ g^{-1}$, respectively. The high surface area of catalyst could enhance the sufficient contact with reactant and provide more reactive sites for efficient catalysis. These results collectively confirmed the formation of Ag species and the intimate contact between Ag and R-MnO_2, which were proposed to be highly beneficial to the catalytic reaction.

The XRD patterns of the as-synthesized samples with different silver loadings are shown in Fig. 2a. All the samples were in well accordance with the standard tetragonal structure of cryptomelane-type MnO_2 (α-MnO_2) (JCPDS 44-0141) [30]. No characteristic diffraction peak belongs to metallic Ag species can be observed in 0.26% and 2.58% Ag/R-MnO_2. This is possibly due to the ultra-small size and high dispersion of silver species on the surface of R-MnO_2. As shown in the XRD patterns in Fig. S6, the weak signal of Ag (111) plane can be observed in 5.63% Ag/R-MnO_2 and 6.83% Ag/R-MnO_2. The Raman spectra of R-MnO_2 and 2.58% Ag/R-MnO_2 are displayed in Fig. 2b. The prominent peaks at around 572 cm^{-1} and 642 cm^{-1} are recognized as the stretching vibration of v_2 (Mn-O) and v_3 (Mn-O) of [MnO_6] groups [31]. For 2.58% Ag/R-MnO_2, the peak red shifts to 637 cm^{-1}. The red shift of Raman peak of Ag/MnO_2 represents the changed Mn—O bond energy and bond lengths due to Ag doping into MnO_2, which indicates the strong interaction between Ag and MnO_2 [32]. This strong interaction between the noble metal and the metal oxide (MMOI) can facilitate the lattice oxygen migration and promote the electron transfer, as well as provide dual active sites at the perimeter between the metal and the metal oxide, thus achieving a high apparent activity [17].

3.2. Chemical states of surface elements

The element states of R-MnO_2 and 2.58% Ag/R-MnO_2 were determined by XPS. The XPS spectra of Mn 2p, O 1s and Ag 3d are shown in Fig. 3, and the corresponding ratio of different oxidation states are summarized in Table 1. As shown in Fig. 3a, XPS spectra of Mn $2p_{3/2}$ of 2.58% Ag/R-MnO_2 are deconvoluted into three peaks with the binding energy at 640.5, 641.6 and 642.7 eV, corresponding to Mn(II), Mn(III) and Mn(IV) with proportions of 12.3%, 39.0% and 48.7%, respectively [11,33]. Notably, the 2.58% Ag/MnO_2 catalyst has a higher proportion of Mn(II) and Mn(III) (51.3%) than that of pristine MnO_2 (40.6%). Moreover, the average oxidation state (AOS) of Mn was calculated based on the XPS spectra of Mn 3s (Fig. S7) in the following formula: AOS $= 8.956 - 1.126\Delta E_s$, where ΔE_s represents the binding energy difference between the two Mn 3s peaks [34]. The AOS of 2.58% Ag/R-MnO_2 is 3.68, which is obviously lower than that of R-MnO_2 (3.81), further confirming much more amount of Mn(II) and Mn(III) species exist in Ag/R-MnO_2. Actually, once a large amount of low valent Mn exists in MnO_2, the Jahn-Teller distortion occurs, resulting in oxygen vacancies to preserve charge conservation [35]. It suggested the existence of oxygen vacancies in Ag/MnO_2 and confirmed that the MMOI between Ag and R-MnO_2 should be greatly formed in Ag/R-MnO_2 based on the principle of electrostatic balance.

As for Ag $3d_{5/2}$ spectra, the binding energy at 368.0 and 367.4 eV can be attributed to Ag(0) and Ag(I) corresponding to the metallic Ag and Ag species bonded to MnO_2, respectively, indicating that the multiple valence states of silver species coexist in 2.58% Ag/R-MnO_2 [36]. The coexistence of Ag(0) and Ag(I) results from our unique synthesis process through photoreduction rather than high temperature treatment or reduction treatment to remove oxygen. The Ag species with mixed valance own enhanced charge mobility that can facilitate the electron replenishment between Ag and MnO_2, and the Ag addition to metal oxide has been reported to activate the lattice oxygen in metal oxide, hence beneficial to catalytic ozonation [36,37].

As shown in Fig. 3b, the O 1s XPS spectra of 2.58% Ag/R-MnO_2 can be deconvoluted into three components with binding energies at 529.9, 531.5 and 532.8 eV, corresponding to the lattice oxygen (O_{latt}), adsorbed oxygen species (O_{ads}) and surface residual water (O_{surf}), respectively [38]. The ratio of lattice oxygen in Ag/R-MnO_2 (72.7%) is significantly

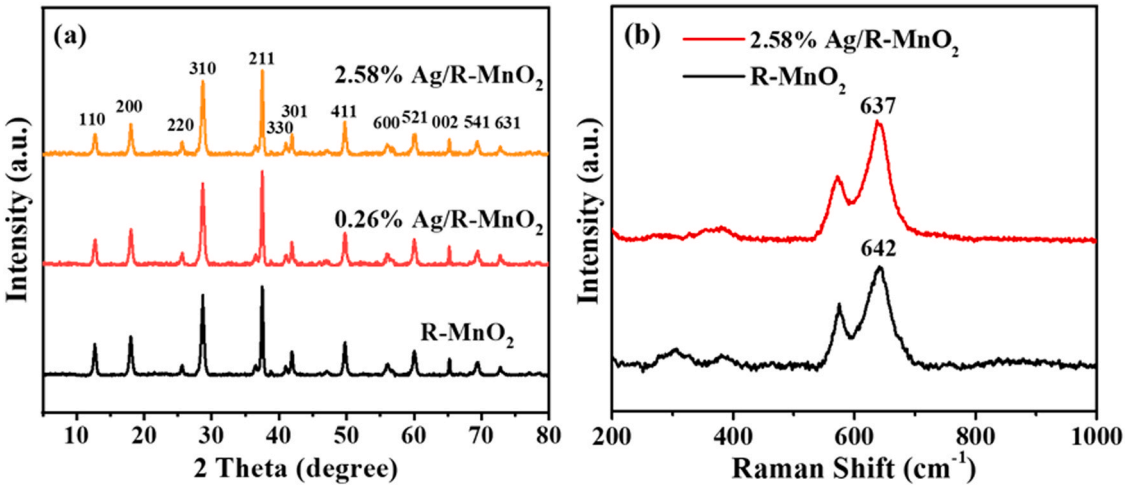

Fig. 2. (a) XRD patterns of R-MnO_2 and Ag/R-MnO_2 with different silver loadings; (b) Raman spectra of R-MnO_2 and 2.58% Ag/R-MnO_2.

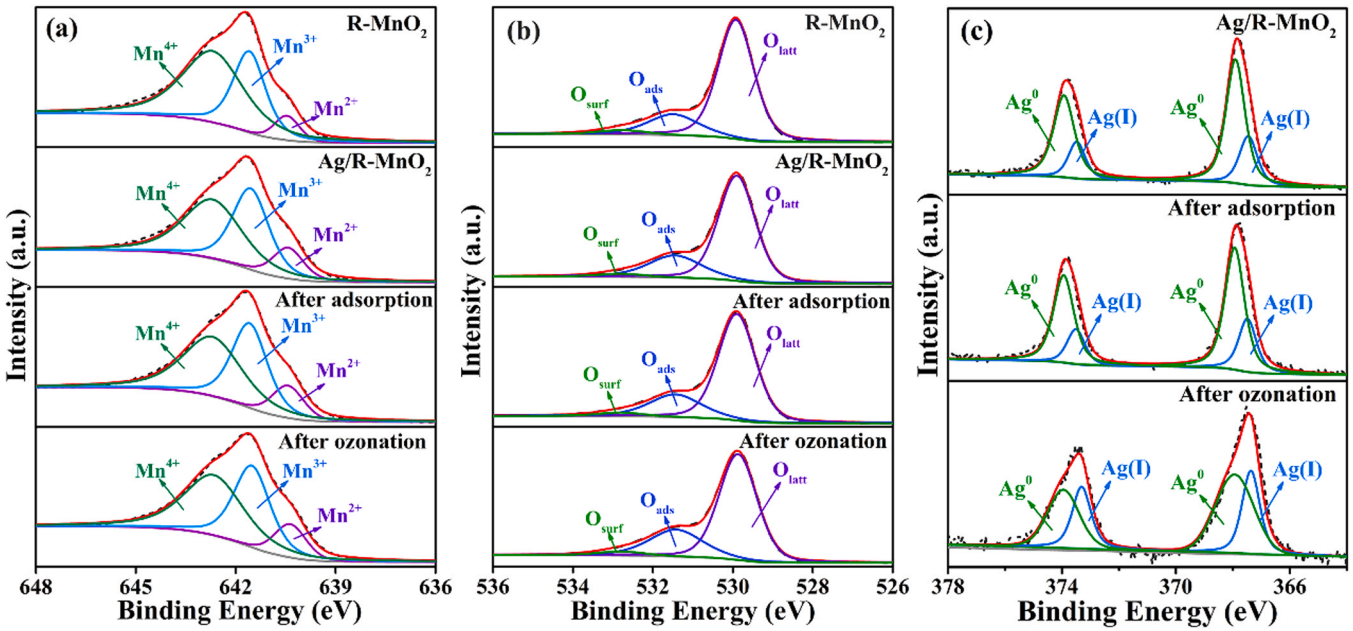

Fig. 3. XPS spectra of (a) Mn $2p_{3/2}$, (b) O 1s and (c) Ag 3d for fresh R-MnO_2, fresh 2.58% Ag/R-MnO_2, 2.58% Ag/R-MnO_2 after adsorption for CH_3SH, and 2.58% Ag/R-MnO_2 after catalytic ozonation for CH_3SH.

Table 1
Chemical and surface compositions of Mn and O in R-MnO_2 and 2.58% Ag/R-MnO_2.

Sample	Mn(II) (%)	Mn(III) (%)	Mn(Ⅳ) (%)	O_{latt} (%)	O_{ads} (%)	O_{surf} (%)	Ag(0) (%)	Ag(I) (%)	Mn(II) + Mn(III)/ Mn(Ⅳ)	O_{latt}/ O_{ads}	Ag(0)/Ag (I)
MnO_2	6.9	33.7	59.4	76.0	20.2	3.8	–	–	0.7	3.8	–
2.58% Ag/R-MnO_2	12.3	39.0	48.7	72.7	24.3	3.0	73.2	26.8	1.1	3.0	2.7
After adsorption (2.58% Ag/R-MnO_2)	12.2	39.3	48.4	72.9	23.7	3.4	71.6	28.4	1.1	3.1	2.5
After ozonation (2.58% Ag/R-MnO_2)	12.2	38.4	49.4	69.6	26.8	3.6	62.4	37.6	1.0	2.6	1.7

lower than that of pristine R-MnO_2 (76.0%). The results suggest the existence of oxygen vacancies in Ag/R-MnO_2, which are formed after Ag deposition [30]. The abundant oxygen vacancies in Ag/R-MnO_2 could result in better adsorption of surface oxygen species [39]. Whereupon Ag/R-MnO_2 demonstrates a higher adsorption of surface oxygen species (O_{ads}) with ratio of 24.3% compared with pristine R-MnO_2 (20.2%), thus facilitating the generation of abundant surface adsorbed oxygen (O^{2-}, O^-, OH^-) to enhance the catalytic reactions [40,41]. Thus, the multivalent Ag species and the oxygen vacancies in Ag/R-MnO_2 are confirmed.

3.3. Surface reducibility and oxygen mobility

The reducibility of ozonation catalysts was investigated by H_2-TPR

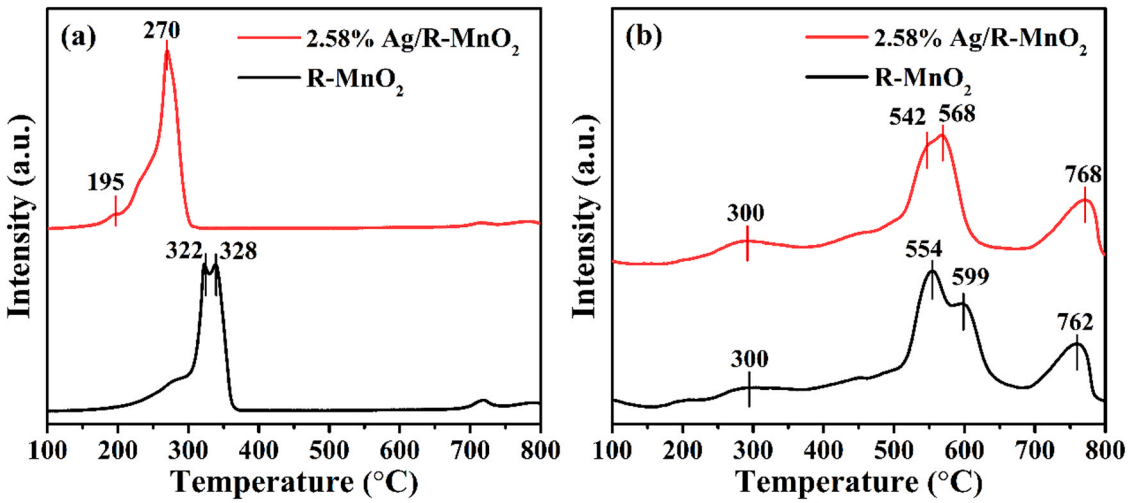

Fig. 4. (a) H_2-TPR profiles and (b) O_2-TPD profiles of R-MnO_2 and 2.58% Ag/R-MnO_2.

experiments, which is an important factor correlated with their redox activity. Moreover, the interaction between Ag species and MnO_2 can also be revealed. As shown in Fig. 4a, the pristine R-MnO_2 shows a wide reduction profile in the range of 310–350 °C, corresponding to the reduction from MnO_2 to MnO with Mn_2O_3 and Mn_3O_4 as intermediates [42]. As for 2.58% Ag/R-MnO_2, the reduction peak position shifts significantly to lower temperature (center at 270 °C), confirming the enhanced reducibility of MnO_2 in Ag/R-MnO_2 [36]. It is reported that silver incorporation can significantly improve the reducibility of MnO_x via the spillover of hydrogen from the silver atoms to the manganese oxides [43]. In addition, the Ag incorporation not only dramatically decreases the main reduction temperature of R-MnO_2 but also gives rise to a new reduction peak around 195 °C corresponding to the reduction of silver oxide species. Notably, the quantified H_2 consumption for 2.58% Ag/R-MnO_2 is 10.63 mmol/g, which is lower than that of R-MnO_2 (11.81 mmol/g). These results are in good agreement with the above XPS results, revealing that deposition of Ag leads to the introduction of oxygen vacancies into R-MnO_2 [44]. It has been reported that oxygen vacancies can strengthen the strong metal-metal oxides interaction, and lead to the stability of metal/metal oxides [45].

Furthermore, O_2-TPD was employed to investigate the oxygen mobility of the as-synthesized catalyst (Fig. 4b). The O_2-TPD process of R-MnO_2 can be divided into three sections. The desorption peak below 400 °C is assigned to the chemisorbed oxygen species and active surface oxygen, while the peak occurred in the range of 450–650 °C can be assigned to the sub-surface lattice oxygen [12,42]. The peaks above 700 °C is contributed by the evolution of bulk lattice oxygen [34]. The larger peak area of 2.58% Ag/R-MnO_2 indicates the amount of the chemisorbed oxygen molecules and active surface oxygen in 2.58% Ag/R-MnO_2 is higher than that of R-MnO_2. Besides, the desorption peak of 2.58% Ag/R-MnO_2 in medium temperature region shifts to lower temperature, indicating 2.58% Ag/R-MnO_2 gives higher oxygen mobility than that of R-MnO_2. [40]. Thus, 2.58% Ag/R-MnO_2 has much more oxygen vacancies and high oxygen mobility, which is expected to possess better catalytic ozonation performance. The perimeter sites at the Ag-MnO_2 interface with oxygen vacancies can act as active sites for catalytic ozonation.

3.4. Catalytic removal of CH_3SH

The catalytic performance of CH_3SH via the as-synthesized samples were evaluated at room temperature in wet catalytic ozonation that combined of wet scrubbing and catalytic ozonation process (Fig. 5a). The CH_3SH dynamic adsorption experiments in the absence of ozone were firstly performed and the results are displayed in Fig. S8. It was observed that 2.58% Ag/R-MnO_2 attains a CH_3SH removal efficiency of 10.4% in gas-solid reaction process in 30 min due to the adsorption of CH_3SH by Ag/R-MnO_2. However, the CH_3SH removal efficiency under wet scrubbing system reaches the maximum of 70.8% at 10 min mainly due to the dissolution of CH_3SH into water. Meanwhile, the similar CH_3SH removal behavior in the absence of Ag/R-MnO_2 catalyst under the wet scrubbing process was observed, indicating that the dissolution

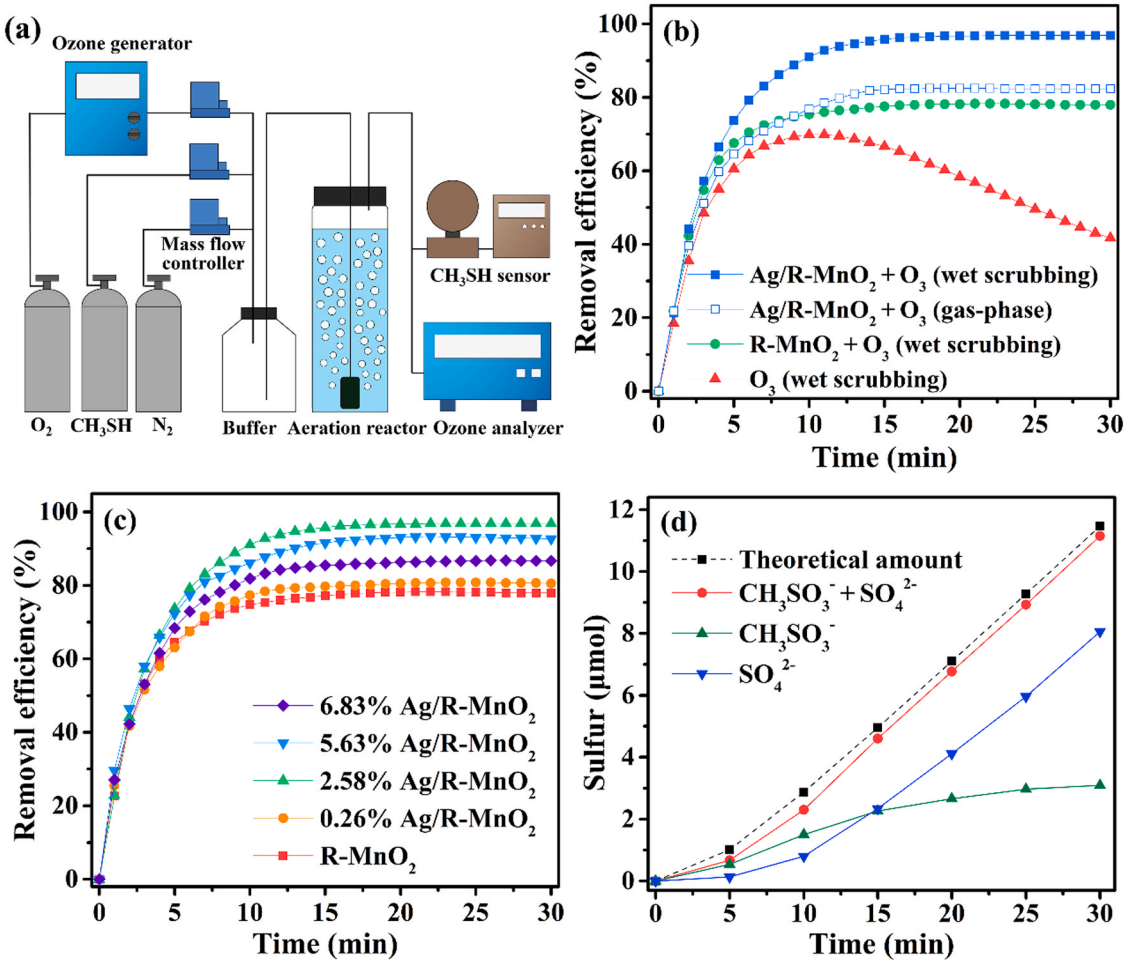

Fig. 5. (a) Schematic diagram of experiment system; (b) Comparison of CH_3SH removal efficiency in wet scrubbing system and gas-solid reaction process; (c) Influence of silver loadings on CH_3SH removal efficiency; (d) Formation of sulfur-containing products in liquid phase during catalytic ozonation process. ($[CH_3SH]_0$ = 75 ppm, $[O_3]_0$ = 30 ppm, catalyst amount = 120 mg, gas flow = 150 mL min^{-1}, 20 °C).

process in wet scrubbing is favorable for CH_3SH enrichment. Subsequently, the removal efficiency sharply decreased over prolonged time due to the saturated dissolution of CH_3SH in water.

After the adsorption equilibrium was attained, the catalytic ozonation performance of the as-synthesized catalysts at room temperature was performed. As shown in Fig. 5b, 2.58% Ag/R-MnO_2 exhibited excellent CH_3SH removal efficiency of 96.9% in coupling process of catalytic ozonation and wet scrubbing, which was significantly higher than that of pure R-MnO_2 (78.0%) and sole ozonation (41.7%). Notably, the turnover frequency (TOF) of 2.58% Ag/R-MnO_2 was calculated to be 92.9 μmol g^{-1} h^{-1}, which was 1.7 times higher than that of R-MnO_2 (53.3 μmol g^{-1} h^{-1}). This is attributed to the advantages of the unique hierarchical composition of Ag/R-MnO_2 with multiple valence states and MMOI that facilitate the dynamic electron replenishment. Notably, the removal rate of 2.58% Ag/R-MnO_2 in the wet catalytic ozonation process was higher than that in the gas phase (82.3%), indicating that the wet catalytic ozonation process exhibits higher effectiveness and has great potential application prospects in the removal of sulfur-containing volatile organic compounds.

The catalytic ozonation performance of Ag/R-MnO_2 catalysts with different silver loadings was shown in Fig. 5c. 2.58% Ag/R-MnO_2 realized the optimum CH_3SH removal efficiency (96.9%) among the as-prepared Ag/R-MnO_2. The further increase of Ag amount could have a negative effect on the catalytic performance. This is because excessive Ag loading might cover the active sites of MnO_2 surface and destroy the 3D rambutan-like MnO_2 hollow structure (Fig. S4). Therefore, the optimized Ag/R-MnO_2 catalyst with a sliver loading of 2.58% was chosen as the default catalyst for subsequent experiments.

To further clarify the mineralization content of CH_3SH, ion chromatography (IC) was performed to clarify the variation of product during wet catalytic ozonation of CH_3SH by Ag/R-MnO_2. As shown in Fig. 5d, two main oxidized products methyl sulfonic acid ion ($CH_3SO_3^-$) and sulfate ion (SO_4^{2-}) were detected. The yield of $CH_3SO_3^-$ increased quickly in first 20 min and then eventually levelled off, whereas the yield of SO_4^{2-} increased rapidly, indicating the intermediate $CH_3SO_3^-$ was oxidized into SO_4^{2-} after 20 min. The total amount of oxidized sulfur products detected was 11.15 μmol after 30 min, which is 97.3% of the theoretical value of introduced CH_3SH (11.45 μmol), and the yield of SO_4^{2-} reaches 8.06 μmol, accounting for 72.3% of the total sulfur. The results confirmed that the Ag/R-MnO_2 system are sufficient to deeply oxidized CH_3SH into SO_4^{2-}, thus achieving the complete oxidation of sulfur and minimizing the secondary pollution.

To further identify the ozone utilization efficiency, the ozone concentration in the exhaust gas was monitored. As shown in Fig. 6a, 25.3% and 85.0% of ozone in feed gas was depleted without and with R-MnO_2 in deionized water in 30 min. Notably, 92.3% utilization rate of ozone was achieved by Ag/R-MnO_2. The high ozone conversion was achieved by Ag/R-MnO_2 can minimize the O_3 pollution. Given that the ozone concentration is also one of the important factors affecting the catalytic ozonation activity [46], the effect of ozone inlet concentration on CH_3SH removal efficiency was investigated as shown in Fig. 6b. The catalytic ozonation performance was significantly enhanced when the ozone inlet concentration increased from 10 to 30 ppm. However, the further increasing of the ozone concentration from 30 to 40 ppm has a negligible effect on the catalytic performance, due to the limited mass transfer of ozone and insufficient contact with catalyst. Hence, the

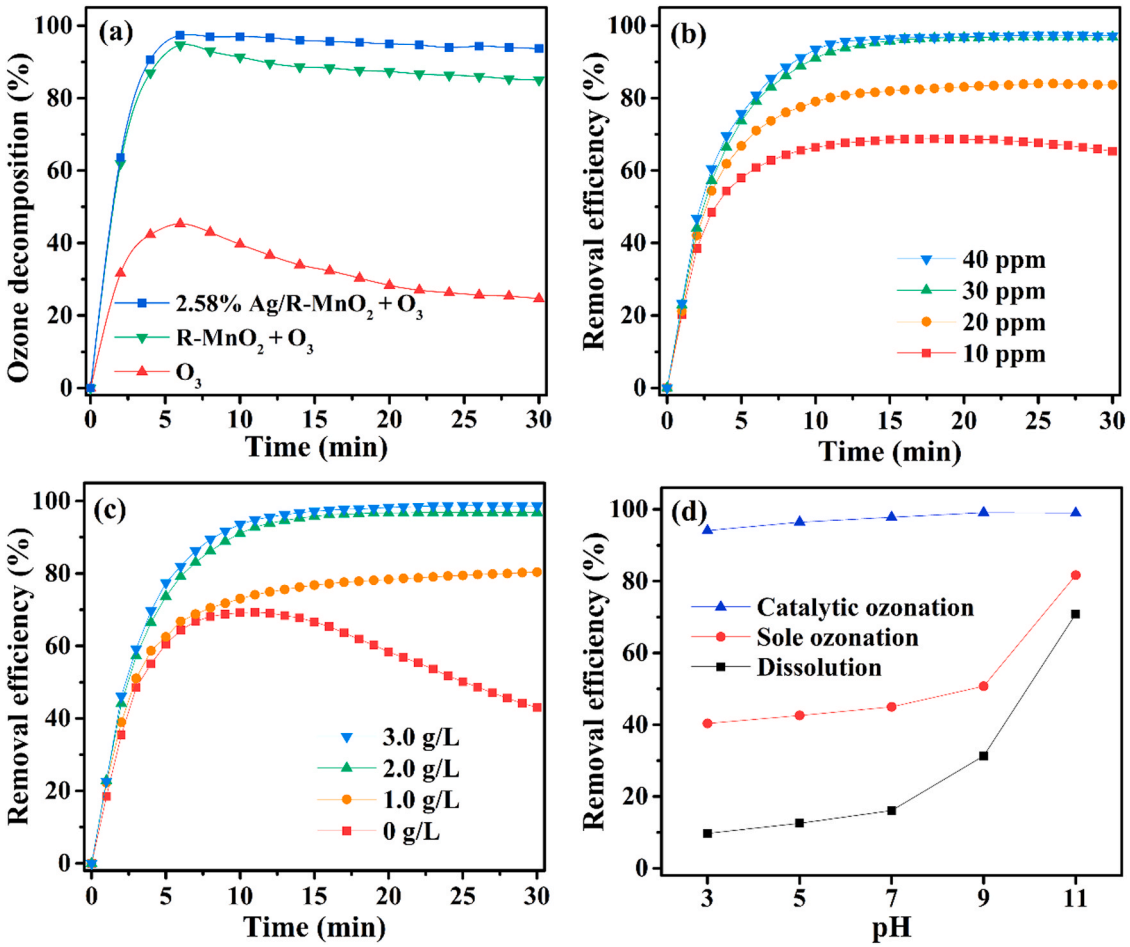

Fig. 6. (a) Ozone decomposition in different system; Influence of (b) ozone inlet concentration, (c) catalyst dosage, and (d) initial pH on CH_3SH removal efficiency. ($[CH_3SH]_0$ = 75 ppm, $[O_3]_0$ = 30 ppm, catalyst amount = 120 mg, gas flow = 150 mL min^{-1}, 20 °C).

optimum O_3 concentration for catalytic ozonation in Ag/R-MnO_2 system is chosen as 30 ppm. In most of the recent reports, the molar ratio of ozone to VOCs is rather high, some even up to 10 to achieve a high VOCs removal efficiency, leading to low ozone utilization rate and excess ozone emission [47]. In our case, the molar ratio of O_3/CH_3SH under 30 ppm O_3 concentration in Ag/R-MnO_2 system was calculated to be 0.4, which was relatively low than the reported ratio. These results collectively confirmed the extremely high ozone utilization of Ag/R-MnO_2, thus avoiding the excessive supply of ozone and reducing ozone emission.

Fig. 6c shows the effect of catalyst dosage on CH_3SH removal efficiency. With the increase of catalyst dosage from 0.1, 0.2, and 0.3 g/L, the removal efficiency of CH_3SH increased from 80.4%, 96.9%, and 98.7%. Although the supply of more catalysts leads to slightly higher CH_3SH removal efficiency, the excessive catalyst leads to low utilization of reactive sites and high cost of catalyst. Therefore, 0.2 g/L of Ag/R-MnO_2 is chosen as the optimum catalyst dosage.

Considering pH may affect the wet catalytic ozonation of CH_3SH, the influence of pH on the catalytic activity was tested at the initial scrubbing solution pH of 3.0, 5.0, 7.0, 9.0 and 11.0, respectively (Fig. 6d). As initial pH increased from 3.0 to 11.0, the dissolution of CH_3SH was dramatically improved to 70.8% at pH = 11.0, as CH_3SH could dissociate as CH_3S^- in alkaline solution (pK_a = 9.7) as described by the equation: $CH_3SH\ (aq) + OH^- \rightleftarrows CH_3S^- + H_2O$ [48]. However, the CH_3SH removal efficiency by Ag/R-MnO_2 in wet catalytic ozonation only slightly increased from 94.1% to 99.0% with the increase of pH from 3.0 to 11.0, indicating this reaction process is robust under a wide range of pH values. This is because the oxidation rate of CH_3SH in this process is greater than the dissolution rate, thus avoiding the saturated adsorption and driving the continuous CH_3SH dissolution. The results indicate the Ag/R-MnO_2 wet catalytic ozonation system are efficient for catalytic oxidation of CH_3SH in a wide pH range.

3.5. Stability of Ag/R-MnO_2 catalyst

Considering that the catalytic stability of a catalyst is critical in view of practical application, the long-term stability of 2.58% Ag/R-MnO_2 in wet catalytic ozonation of CH_3SH was evaluated and compared with that in gaseous system. As shown in Fig. 7a, Ag/R-MnO_2 displayed an excellent stability for CH_3SH oxidation in wet catalytic ozonation, with a removal efficiency remaining ~ 93% for 4 h on-stream period. Obviously, the wet catalytic ozonation is able to maintain well stability for continuous removal of CH_3SH, whereas CH_3SH removal efficiency of Ag/R-MnO_2 in gas-solid system drastically declined from 82.5% to 70.2% after 4 h reaction due to the catalyst deactivation. The deactivation of Ag/R-MnO_2 in the gas-solid system may be ascribed to the accumulation of carbon and sulfur species on catalyst surface that covers the reaction active sites. Thus, the mass transfer of reactants was enhanced by the wet catalytic ozonation process and the accumulation products on the catalyst surface was prevented via continuous dissolution, achieving remarkable long-term catalytic performance. Catalytic activity comparison of Ag/R-MnO_2 with that of previously reported catalysts are listed in Table S2, revealing the superior catalytic performance of Ag/R-MnO_2. The recyclability of Ag/R-MnO_2 is tested by a five-run recycling experiment (Fig. S9). The catalyst can be separated from the reaction mixture by simple filtration for reusing in the next run. Every batch was carried out under the same reaction conditions. The activity of the catalyst is kept constant after five-run recycling, which indicates the excellent recyclability of Ag/R-MnO_2 catalyst.

The accumulation of products and intermediates on the surface of used catalysts after reaction for 30 min was further investigated by FTIR. The catalysts after long-term reaction were collected without any regeneration treatment. As shown in Fig. 7b, in wet catalytic ozonation system, only a slight amount of carbon and sulfur-containing surface groups was observed on the used Ag/R-MnO_2 catalyst, indicating that the number of residual products and intermediates existed on the catalyst surface can be ignored. However, with respect to gas-solid system, the residual reaction intermediates such as carbonaceous species (1408 cm^{-1}, 1571 and 1330 cm^{-1}) and sulfur-containing species (1176, 1050, 976 and 928 cm^{-1}) on Ag/R-MnO_2 catalyst can be observed clearly after catalytic ozonation [49–51]. Water in wet-scrubbing reactor promotes the mass transfer of reactants and dissolves, washes and carries away the products on the catalyst surface, preventing the accumulation thus regenerating the catalyst. Therefore, the wet catalytic ozonation system that combines wet scrubbing and catalytic ozonation can realize the rapid and long-term stable oxidation of CH_3SH.

3.6. Role of active sites and oxygen species

Upon confirming the superior catalytic performance in Ag/R-MnO_2 system, the active sites and reactive species are further explored to clarify the catalytic mechanism. With electron-rich structure, ozone molecules are prone to be adsorbed on the electron deficient sites of the catalyst, such as the Lewis acid sites [52]. It has been reported that phosphate forms strongly bonds with the surface Lewis acid sites of the catalyst [53]. Thus, the role of Lewis acid sites of Ag/R-MnO_2 during catalytic ozonation was determined by using sodium dihydrogen phosphate as the probe. As shown in Fig. 8a, the removal of CH_3SH by Ag/R-MnO_2 was obviously suppressed after adding phosphate, and the removal efficiency decreased from 96.9% to 61.4%. This indicates that

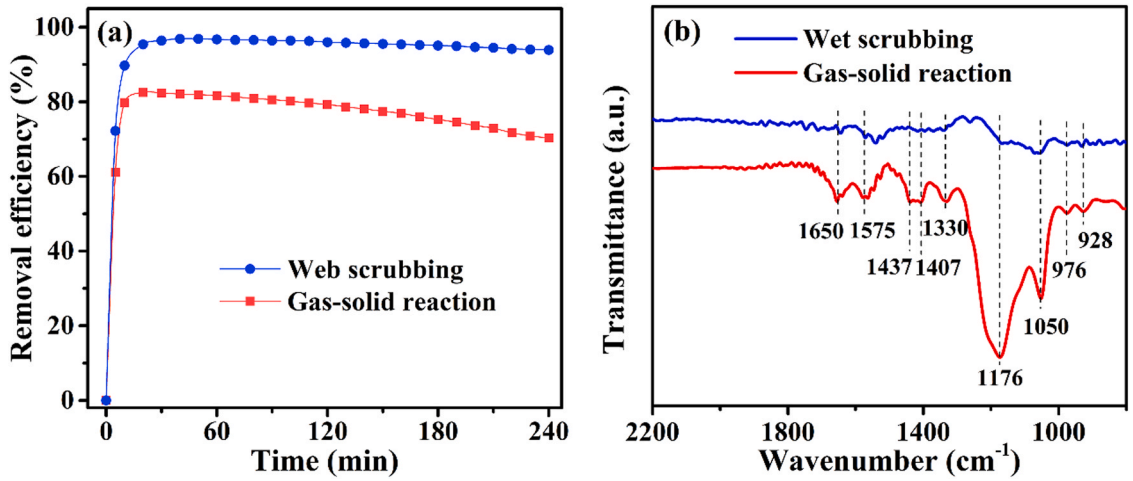

Fig. 7. (a) Stability of Ag/R-MnO_2 in wet scrubbing system and gas-solid reaction process; (b) FTIR spectra of used Ag/R-MnO_2 after reaction. ($[CH_3SH]_0$ = 75 ppm, $[O_3]_0$ = 30 ppm, catalyst amount = 120 mg, gas flow = 150 mL min^{-1}, 20 °C).

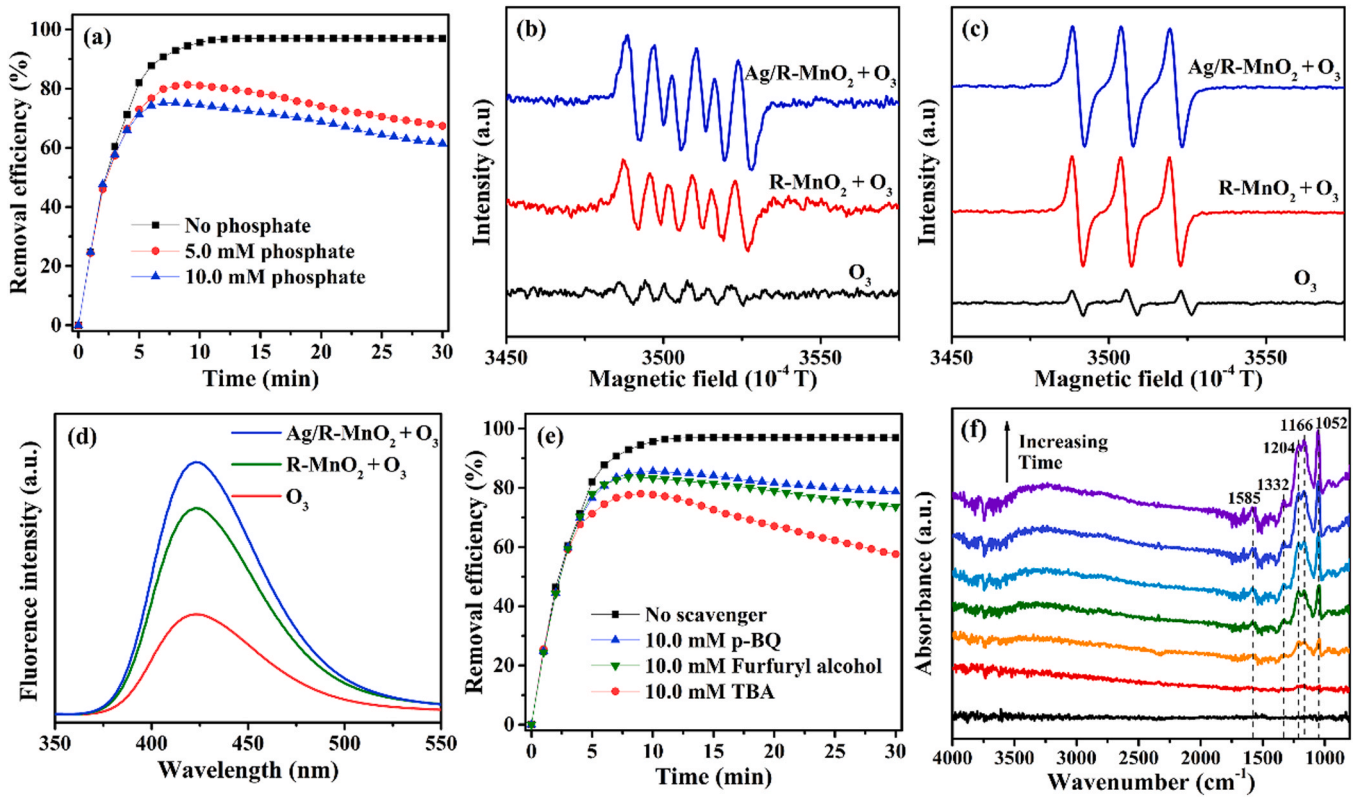

Fig. 8. (a) Catalytic ozonation of Ag/R-MnO_2 for CH_3SH with addition of phosphate as Lewis acid sites probe; ESR spectra of (b) $\bullet O_2^-$ and (c) $^1O_2$ using DMPO and TEMP as trapping agents, respectively; (d) Fluorescence spectra of different system in catalytic ozonation; (e) Catalytic ozonation of Ag/R-MnO_2 for CH_3SH with addition of different scavengers; (f) In situ ATR-FTIR spectra of catalytic ozonation of Ag/R-MnO_2 for CH_3SH. ($[CH_3SH]_0 = 75$ ppm, $[O_3]_0 = 30$ ppm, catalyst amount = 120 mg, gas flow = 150 mL min^{-1}, 20 °C).

Lewis acid sites were the main active center of Ag/R-MnO_2 in wet catalytic ozonation. Usually, the surface oxygen vacancies in metal oxides are widely recognized as the Lewis acid sites to activate ozone molecules [54]. As confirmed by XPS and H_2-TPR results, the incorporation of Ag in MnO_2 matrix via the photoreduction leads to the formation of much more oxygen vacancies (Figs. 3 and 4a). Thus, Ag/R-MnO_2 with abundant oxygen vacancies as the Lewis acid sites enables to convert more O_3 molecules into reactive species for rapid oxidation of CH_3SH.

The reactive species in Ag/R-MnO_2 wet catalytic ozonation system were identified by Electron spin resonance (ESR). As shown in Fig. 8b, c, both superoxide radical ($\bullet O_2^-$) and singlet oxygen ($^1O_2$) were observed in sole ozonation, R-MnO_2 and Ag/R-MnO_2 systems during catalytic ozonation, while Ag/R-MnO_2 system shows the strongest signals. Since the detection of hydroxyl radical (•OH) by ESR can be disturbed by manganese species (Fig S7), the fluorescence probe methods were applied with terephthalic acid as the fluorescent probe [46]. As shown in Fig S8, the fluorescence intensity increases with time during the catalytic ozonation in Ag/R-MnO_2 system, shows the rapid generation of •OH. Moreover, the fluorescence intensity of Ag/R-MnO_2 system was significantly higher than that of R-MnO_2 system and sole ozonation (Fig. 8d), confirming Ag/R-MnO_2 system promoted •OH generation. To further investigate the contribution of reactive oxygen species for CH_3SH removal during catalytic ozonation, the radicals scavenging experiment were performed. Tert-butanol (TBA) is known as an effective •OH scavenger, with a reaction rate constant of 5.0×10^8 $M^{-1}s^{-1}$ for •OH and 3.0×10^{-3} M^{-1} s^{-1} for O_3 [55]. Meanwhile, p-benzoquinone and furfuryl alcohol were selected as the $\bullet O_2^-$ and $^1O_2$ scavengers, respectively [56,57]. As shown in Fig. 8e, the addition of TBA dramatically inhibited the removal efficiency of CH_3SH by 39.3%, while p-benzoquinone and furfuryl alcohol were suppressed by 18.2% and 23.3%, respectively. This suggests the •OH is the dominant ROSs for CH_3SH oxidation in Ag/R-MnO_2 wet scrubbing system.

3.7. Mechanism of wet catalytic ozonation for CH_3SH degradation

To deepen the comprehension in the reaction mechanism of CH_3SH over Ag/R-MnO_2, we investigated the chemical state change of used Ag/R-MnO_2 after 30 min reaction using XPS. After adsorption, the relative molar ratio of Ag(0)/Ag(I) decreased slightly from 2.7 to 2.5 (Fig. 3c and Table 1). Due to the strong affinity of Ag to thiols, the S—H bond of CH_3SH dissociated and the deprotonated alkane thiolate species such as CH_3S-Ag formed, leading to the chemisorption of CH_3SH on catalysts surface [58]. After wet catalytic ozonation, Ag(0)/Ag(I) ratio of Ag/R-MnO_2 decreased from 2.5 to 1.7, while Mn(II) + Mn(III)/Mn(IV) ratio almost remained unchanged. Notably, the Mn(II) + Mn(III)/Mn(IV) ratio of bare MnO_2 after catalytic ozonation was significantly decreased (by 24%) as reported in our previous works [39]. Typically, the multivalent MnO_2 is the primary electron donor via the transfer of ≡Mn(II)/Mn(III) → ≡Mn(IV) to activate ozone into ROSs. The relatively stable molar ratio of Mn(II) + Mn(III)/Mn(IV) in Ag/R-MnO_2 during the adsorption and reaction stage suggests a spontaneous electron transfer from Ag(0) to MnO_2 based on the strong MMOI effect, thus to induce the dynamically balanced Mn(II) + Mn(III)/Mn(IV) ratio. Such redox shuttle is essential to maintain the catalytic activity stability of Ag/R-MnO_2 during catalytic ozonation.

Furthermore, in situ DRIFT spectroscopy was employed to monitor reaction process (Fig. 8f). The characteristic peaks at 1204 and 1166 cm^{-1} assigned to stretching vibrations of S—O and 1050 cm^{-1} assigned to S═O derived from $CH_3SO_3^-$ and SO_4^{2-} gradually increased over time, indicating CH_3SH are efficiently oxidized into $CH_3SO_3^-$ and SO_4^{2-} [51]. In addition, carboxylate species (1585 cm^{-1}) and carbonate species (1332 cm^{-1}) were also detected and increased slightly with time,

owing to the release of carbonaceous species into aqueous solution [49]. The results are consistent with the above-mentioned result of IC experiment, indicating the reactive species formed in Ag/R-MnO_2/O_3 system are sufficient to deeply oxidized CH_3SH to final products (CO_3^{2-} and SO_4^{2-}).

Based on the results and discussions above, a possible pathway of wet catalytic ozonation of CH_3SH by Ag/R-MnO_2 were proposed and are shown in Fig. 9. Firstly, the gaseous CH_3SH was dissolved in aqueous solution. Subsequently, the CH_3SH molecules were adsorbed onto the surface of Ag/R-MnO_2. Meanwhile, ozone molecules were trapped in the oxygen vacancies of Ag/R-MnO_2 and activated into reactive oxygen species (ROSs) to decompose the adjacent chemisorbed CH_3SH (Eqs. (1)–(6)). The conversion of Mn(II)/Mn(III) to Mn(IV) donated electrons for sustainable catalytic ozonation, and the consumed electrons of MnO_2 are replenished via charge-transfer of Ag(0) → Ag(I) (Eq. (7)), resulting in a high apparent activity. Meanwhile, the transfer of O_{Latt} → O_2 maintained the electrostatic balance of Ag, which can be evidenced by the high oxygen mobility (Fig. 4b) and the slight decrease of O_{latt} species observed in Ag/R-MnO_2 after reaction (Table 1) [39]. The MMOI between Ag and R-MnO_2 facilitates the electrons transfer and O_{Latt} migration in Ag/R-MnO_2 (Eqs. (7) and (8)), thus maintaining the redox stability of catalyst [17,59]. Meanwhile, the oxidative products such as CO_3^{2-} and SO_4^{2-}, which are released from the catalyst surface to the aqueous solution, finally, ensuring the long-term stability of the catalyst.

$$\equiv Mn(II)/Mn(III)\text{-}O(V_O) + H_2O \rightarrow \equiv Mn(II)/Mn(III)\text{-}(OH)_2 \quad (1)$$

$$\equiv Mn(II)/Mn(III)\text{-}OH + O_3 \rightarrow \equiv Mn(IV) + \cdot O_2^- + \cdot HO_2 \quad (2)$$

$$\cdot HO_2 + O_3 \rightarrow \cdot OH + 2O_2 \quad (3)$$

$$\cdot O_2^- + \cdot OH \rightarrow {}^1O_2 + OH^- \quad (4)$$

$$CH_3SH + \cdot OH \text{ or } {}^1O_2 \text{ or } \cdot O_2^- \rightarrow CH_3SO_3^- + H_2O \quad (5)$$

$$CH_3SO_3^- + \cdot OH \text{ or } {}^1O_2 \text{ or } \cdot O_2^- \rightarrow SO_4^{2-} + CO_3^{2-} \text{ or } CO_2 \quad (6)$$

$$\equiv Mn(IV) + Ag(0) \rightarrow \equiv Mn(II)/Mn(III) + \equiv Ag(I) \quad (7)$$

$$\equiv Mn(IV) + \equiv Ag(I) + 2\,O_{latt} \rightarrow \equiv Mn(II)/Mn(III) + Ag(0) + O_2 \quad (8)$$

4. Conclusion

In this study, the mixed valence Ag were supported on the rambutan-like MnO_2 hollow microspheres (Ag/R-MnO_2) with strong metal–metal oxide interaction (MMOI) was successfully developed for the elimination of CH_3SH in a wet scrubbing coupled with catalytic ozonation at ambient temperature. A satisfied CH_3SH removal efficiency of 96.9% (TOF = 92.9 μmol g^{-1} h^{-1}) and a high O_3 utilizing efficiency (92.3%) with long-term stability up to 4 h were achieved by 2.58% Ag/R-MnO_2, which outperformed the pristine R-MnO_2 and sole ozonation. SO_4^{2-} and CO_3^{2-} were identified as the main final products of catalytic ozonation of Ag/R-MnO_2 for CH_3SH. The impressive catalytic ozonation performance of Ag/R-MnO_2 can be attributed to the following synergistic effects: (a) the MMOI effect of Ag/R-MnO_2 plays a critical role not only in facilitating the dynamically replenishing electron from the Ag(0)/Ag(I) to R-MnO_2 for stabilizing the valence state of Mn, but also promoting the lattice oxygen migration to achieve a high apparent activity, (b) the role of oxygen vacancies in MnO_2 in achieving efficient decomposition of ozone to ROSs; (c) the wet scrubbing system promotes the mass transfer of reactants and products during catalytic ozonation to avoid their accumulation on the catalyst surface, thus realizing the long-term stable oxidation of CH_3SH. Our work presents a new strategy for boosting ozone activation and eliminating S-VOCs under mild condition through redox-robust shuttle of catalyst in wet scrubbing coupled with catalytic ozonation technology.

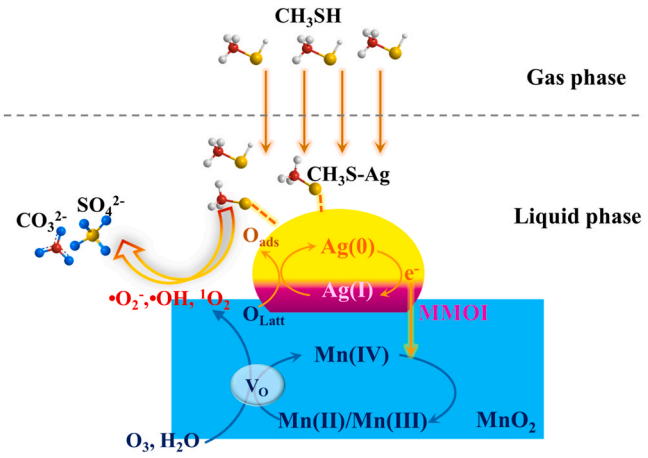

Fig. 9. A possible pathway for degradation of CH_3SH.

CRediT authorship contribution statement

Chun He: Writing – review & editing, Supervision, Funding acquisition. **Yuhong Liao**: Conceptualization, Investigation, Writing – original draft, Writing – review & editing. **Cheng Chen**: Investigation, Visualization, Formal analysis. **Dehua Xia**: Supervision, Funding acquisition. **Yongyi Wang:** Investigation. **Shuanghong Tian:** Investigation. **Jingling Yang:** Conceptualization, Investigation. **Dong Shu:** Visualization, Analysis.

Declaration of Competing Interest

The authors declare that they have no known competing financial interests or personal relationships that could have appeared to influence the work reported in this paper.

Acknowledgments

The authors wish to thank the National Natural Science Foundation of China (Nos. 21876212, 21976214, 41603097, 22006051, 21673086 and 52070195), Science and Technology Research Programs of Guangdong Province (No. 2019A1515011015), the Science and Technology Program of Guangzhou (No. 201904010353), and Fundamental Research Funds for the Central Universities (No. 19lgpy157) for financially supporting this work.

Appendix A. Supplementary material

Supplementary data associated with this article can be found in the online version at doi:10.1016/j.apcatb.2021.120881.

References

[1] Y.-S. Son, J.-C. Kim, Decomposition of sulfur compounds by radiolysis: I. Influential factors, Chem. Eng. J. 262 (2015) 217–223.
[2] J. Yang, Q. Zhang, F. Zhang, D. Xia, H. Liu, S. Tian, L. Sun, D. Shu, C. He, S. Runa, Three-dimensional hierarchical porous sludge-derived carbon supported on silicon carbide foams as effective and stable Fenton-like catalyst for odorous methyl mercaptan elimination, J. Hazard. Mater. 358 (2018) 136–144.
[3] X. Ma, H. Liu, W. Li, S. Peng, Y. Chen, Reactive adsorption of low concentration methyl mercaptan on a Cu-based MOF with controllable size and shape, RSC Adv. 6 (2016) 96997–97003.
[4] L. Ding, H.-C. Liang, X.-Z. Li, Oxidation of CH3SH by in situ generation of ferrate (VI) in aqueous alkaline solution for odour treatment, Sep. Purif. Technol. 91 (2012) 117–124.
[5] R.C. van Leerdam, F.A. de Bok, B.P. Lomans, A.J. Stams, P.N. Lens, A.J. Janssen, Volatile organic sulfur compounds in anaerobic sludge and sediments: biodegradation and toxicity, Environ. Toxicol. Chem. 25 (2006) 3101–3109.
[6] S.Z. Zhao, H.H. Yi, X.L. Tang, F.Y. Gao, B.W. Zhang, Z.X. Wang, Y.R. Zuo, Methyl mercaptan removal from gas streams using metal-modified activated carbon, J. Clean. Prod. 87 (2015) 856–861.

[7] D. He, G. Wan, H. Hao, D. Chen, J. Lu, L. Zhang, F. Liu, L. Zhong, S. He, Y. Luo, Microwave-assisted rapid synthesis of CeO2 nanoparticles and its desulfurization processes for CH3SH catalytic decomposition, Chem. Eng. J. 289 (2016) 161–169.

[8] C. He, J. Cheng, X. Zhang, M. Douthwaite, S. Pattisson, Z. Hao, Recent advances in the catalytic oxidation of volatile organic compounds: a review based on pollutant sorts and sources, Chem. Rev. 119 (2019) 4471–4568.

[9] J. Vittenet, W. Aboussaoud, J. Mendret, J.-S. Pic, H. Debellefontaine, N. Lesage, K. Faucher, M.-H. Manero, F. Thibault-Starzyk, H. Leclerc, A. Galarneau, S. Brosillon, Catalytic ozonation with γ-Al2O3 to enhance the degradation of refractory organics in water, Appl. Catal. A Gen. 504 (2015) 519–532.

[10] X. Tan, Y. Wan, Y. Huang, C. He, Z. Zhang, Z. He, L. Hu, J. Zeng, D. Shu, Three-dimensional MnO2 porous hollow microspheres for enhanced activity as ozonation catalysts in degradation of bisphenol A, J. Hazard. Mater. 321 (2017) 162–172.

[11] F. Wang, H. Dai, J. Deng, G. Bai, K. Ji, Y. Liu, Manganese oxides with rod-, wire-, tube-, and flower-like morphologies: highly effective catalysts for the removal of toluene, Environ. Sci. Technol. 46 (2012) 4034–4041.

[12] J.B. Jia, P.Y. Zhang, L. Chen, Catalytic decomposition of gaseous ozone over manganese dioxides with different crystal structures, Appl. Catal. B Environ. 189 (2016) 210–218.

[13] J. Nawrocki, Catalytic ozonation in water: controversies and questions. Discussion paper, Appl. Catal. B Environ. 142 (2013) 465–471.

[14] E. Sahle-Demessie, V.G. Devulapelli, Oxidation of methanol and total reduced sulfur compounds with ozone over V2O5/TiO2 catalyst: effect of humidity, Appl. Catal. A Gen. 361 (2009) 72–80.

[15] Q.Y. Jia, J.S. Ghoshal, J.K. Li, W.T. Liang, G.N. Meng, H.Y. Che, S.M. Zhang, Z. F. Ma, S. Mukerjee, Metal and metal oxide interactions and their catalytic consequences for oxygen reduction reaction, J. Am. Chem. Soc. 139 (2017) 7893–7903.

[16] X.Q. Yang, S.H. Liu, J.W. Li, J.Y. Chen, Z.B. Rui, Promotion effect of strong metal-support interaction to thermocatalytic, photocatalytic, and photothermocatalytic oxidation of toluene on Pt/SrTiO3, Chemosphere 249 (2020) 8.

[17] Y.F. Li, L.J. Xiao, F.F. Liu, Y.S. Dou, S.M. Liu, Y. Fan, G. Cheng, W. Song, J.L. Zhou, Core-shell structure Ag@Pd nanoparticles supported on layered MnO2 substrate as toluene oxidation catalyst, J. Nanopart. Res. 21 (2019) 10.

[18] C.A. Cellier, V. Vromman, V. Ruaux, E.M. Gaigneaux, P. Grange, Sulfation mechanism and catalytic behavior of manganese oxide in the oxidation of methanethiol, J. Phys. Chem. B 108 (2004) 9989–10001.

[19] T.X. Liu, X.Z. Li, F.B. Li, Development of a photocatalytic wet scrubbing process for gaseous odor treatment, Ind. Eng. Chem. Res. 49 (2010) 3617–3622.

[20] M. Tokumura, R. Nakajima, H.T. Znad, Y. Kawase, Chemical absorption process for degradation of VOC gas using heterogeneous gas-liquid photocatalytic oxidation: toluene degradation by photo-Fenton reaction, Chemosphere 73 (2008) 768–775.

[21] R.J. Xie, J. Ji, H.B. Huang, D.X. Lei, R.M. Fang, Y.J. Shu, Y.J. Zhan, K.H. Guo, D.Y. C. Leung, Heterogeneous activation of peroxymonosulfate over monodispersed Co3O4/activated carbon for efficient degradation of gaseous toluene, Chem. Eng. J. 341 (2018) 383–391.

[22] M. Tokumura, Y. Wada, Y. Usami, T. Yamaki, A. Mizukoshi, M. Noguchi, Y. Yanagisawa, Method of removal of volatile organic compounds by using wet scrubber coupled with photo-Fenton reaction–preventing emission of by-products, Chemosphere 89 (2012) 1238–1242.

[23] C.-C. Liu, R. Ramu, S.I. Chan, C.-Y. Mou, S.S.-F. Yu, Chemistry in confined space: a strategy for selective oxidation of hydrocarbons with high catalytic efficiencies and conversion yields under ambient conditions, Catal. Sci. Technol. 6 (2016) 7623–7630.

[24] Y.-B. Huang, J. Liang, X.-S. Wang, R. Cao, Multifunctional metal–organic framework catalysts: synergistic catalysis and tandem reactions, Chem. Soc. Rev. 46 (2017) 126–157.

[25] Y. Liu, M. Zhang, J. Zhang, Y. Qian, A simple method of fabricating large-area α-MnO2 nanowires and nanorods, J. Solid State Chem. 179 (2006) 1757–1761.

[26] D. Guin, S.V. Manorama, J.N.L. Latha, S. Singh, Nanoparticles/nanotubes: synthesis, characterization, and tested for antibacterial outcomephotoreduction of silver on bare and colloidal TiO2, J. Phys. Chem. C 111 (2007) 13393–13397.

[27] C.-K. Tsung, W.B. Hong, Q.H. Shi, X.S. Kou, M.H. Yeung, J.F. Wang, G.D. Stucky, Shape- and orientation-controlled gold nanoparticles formed within mesoporous silica nanofibers, Adv. Funct. Mater. 16 (2006) 2225–2230.

[28] Y.-L. Zhang, L. Guo, H. Xia, Q.-D. Chen, J. Feng, H.-B. Sun, Photoreduction of graphene oxides: methods, properties, and applications, Adv. Opt. Mater. 2 (2014) 10–28.

[29] J. Ohyama, A. Yamamoto, K. Teramura, T. Shishido, T. Tanaka, Modification of metal nanoparticles with TiO2 and metal-support interaction in photodeposition, ACS Catal. 1 (2011) 187–192.

[30] G. Li, Y. Lu, C. Lu, M. Zhu, C. Zhai, Y. Du, P. Yang, Efficient catalytic ozonation of bisphenol-A over reduced graphene oxide modified sea urchin-like α-MnO2 architectures, J. Hazard. Mater. 294 (2015) 201–208.

[31] C.M. Julien, M. Massot, C. Poinsignon, Lattice vibrations of manganese oxides. Part I. Periodic structures, Spectrochim. Acta Part A 60 (2004) 689–700.

[32] B. Bai, Q. Qiao, H. Arandiyan, J. Li, J. Hao, Three-dimensional ordered mesoporous MnO2-supported Ag nanoparticles for catalytic removal of formaldehyde, Environ. Sci. Technol. 50 (2016) 2635–2640.

[33] W.Z. Si, Y. Wang, S. Zhao, F.Y. Hu, J.H. Li, A facile method for in situ preparation of the MnO2/LaMnO3 catalyst for the removal of toluene, Environ. Sci. Technol. 50 (2016) 4572–4578.

[34] X. Li, J. Ma, L. Yang, G. He, C. Zhang, R. Zhang, H. He, Oxygen vacancies induced by transition metal doping in gamma-MnO2 for highly efficient ozone decomposition, Environ. Sci. Technol. 52 (2018) 12685–12696.

[35] Y.F. Yuan, K. He, B.W. Byles, C. Liu, K. Amine, J. Lu, E. Pomerantseva, R. Shahbazian-Yassar, Deciphering the atomic patterns leading to MnO2 polymorphism, Chem 5 (2019) 1793–1805.

[36] J.M. Li, Z.P. Qu, Y. Qin, H. Wang, Effect of MnO2 morphology on the catalytic oxidation of toluene over Ag/MnO2 catalysts, Appl. Surf. Sci. 385 (2016) 234–240.

[37] Y.H. Chen, C.Y. Mou, B.Z. Wan, Ultrasmall gold nanoparticles confined in zeolite Y: preparation and activity in CO oxidation, Appl. Catal. B Environ. 218 (2017) 506–514.

[38] H. Zhao, Y. Dong, P. Jiang, G. Wang, J. Zhang, K. Li, C. Feng, An α-MnO2 nanotube used as a novel catalyst in ozonation: performance and the mechanism, New J. Chem. 38 (2014) 1743–1750.

[39] J. Yang, Y. Huang, Y.-W. Chen, D. Xia, C.-Y. Mou, L. Hu, J. Zeng, C. He, P.K. Wong, H.-Y. Zhu, Active site-directed tandem catalysis on CuO/VO-MnO2 for efficient and stable catalytic ozonation of S-VOCs under mild condition, Nano Today 35 (2020), 100944.

[40] J. Jia, P. Zhang, L. Chen, The effect of morphology of α-MnO2 on catalytic decomposition of gaseous ozone, Catal. Sci. Technol. 6 (2016) 5841–5847.

[41] Y. Yang, J. Jia, Y. Liu, P. Zhang, The effect of tungsten doping on the catalytic activity of α-MnO2 nanomaterial for ozone decomposition under humid condition, Appl. Catal. A Gen. 562 (2018) 132–141.

[42] G. Zhu, J. Zhu, W. Jiang, Z. Zhang, J. Wang, Y. Zhu, Q. Zhang, Surface oxygen vacancy induced α-MnO2 nanofiber for highly efficient ozone elimination, Appl. Catal. B Environ. 209 (2017) 729–737.

[43] Q. Ye, J.S. Zhao, F.F. Huo, J. Wang, S.Y. Cheng, T.F. Kang, H.X. Dai, Nanosized Ag/α-MnO2 catalysts highly active for the low-temperature oxidation of carbon monoxide and benzene, Catal. Today 175 (2011) 603–609.

[44] Y. Liu, W.J. Yang, P.Y. Zhang, J.Y. Zhang, Nitric acid-treated birnessite-type MnO2: an efficient and hydrophobic material for humid ozone decomposition, Appl. Surf. Sci. 442 (2018) 640–649.

[45] J. Humphreys, R. Lan, S.G. Chen, S.W. Tao, Improved stability and activity of Fe-based catalysts through strong metal support interactions due to extrinsic oxygen vacancies in Ce0.8Sm0.2O2-δ for the efficient synthesis of ammonia, J. Mater. Chem. A 8 (2020) 16676–16689.

[46] S. Afzal, X. Quan, J. Zhang, High surface area mesoporous nanocast LaMO3 (M = Mn, Fe) perovskites for efficient catalytic ozonation and an insight into probable catalytic mechanism, Appl. Catal. B Environ. 206 (2017) 692–703.

[47] T. Nothe, H. Fahlenkamp, C. von Sonntag, Ozonation of wastewater: rate of ozone consumption and hydroxyl radical yield, Environ. Sci. Technol. 43 (2009) 5990–5995.

[48] A. Couvert, I. Charron, A. Laplanche, C. Renner, L. Patria, B. Requieme, Treatment of odorous sulphur compounds by chemical scrubbing with hydrogen peroxide-application to a laboratory plant, Chem. Eng. J. 61 (2006) 7240–7248.

[49] L. Zhu, J. Wang, S. Rong, H. Wang, P. Zhang, Cerium modified birnessite-type MnO2 for gaseous formaldehyde oxidation at low temperature, Appl. Catal. B Environ. 211 (2017) 212–221.

[50] H. Einaga, S. Futamura, Catalytic oxidation of benzene with ozone over alumina-supported manganese oxides, J. Catal. 227 (2004) 304–312.

[51] S. Zhao, H. Yi, X. Tang, D. Kang, F. Gao, J. Wang, Y. Huang, Z. Yang, Removal of volatile odorous organic compounds over NiAl mixed oxides at low temperature, J. Hazard. Mater. 344 (2018) 797–810.

[52] W. Li, Z. Qiang, T. Zhang, F. Cao, Kinetics and mechanism of pyruvic acid degradation by ozone in the presence of PdO/CeO2, Appl. Catal. B Environ. 113–114 (2012) 290–295.

[53] A. Lv, C. Hu, Y. Nie, J. Qu, Catalytic ozonation of toxic pollutants over magnetic cobalt and manganese co-doped γ-Fe2O3, Appl. Catal. B Environ. 100 (2010) 62–67.

[54] W.R. Chen, X.K. Li, Z.Q. Pan, S.S. Ma, L.S. Li, Effective mineralization of diclofenac by catalytic ozonation using Fe-MCM-41 catalyst, Chem. Eng. J. 304 (2016) 594–601.

[55] L. Zhao, J. Ma, Z.Z. Sun, Oxidation products and pathway of ceramic honeycomb-catalyzed ozonation for the degradation of nitrobenzene in aqueous solution, Appl. Catal. B Environ. 79 (2008) 244–253.

[56] Y. Ding, X. Xia, Y. Ruan, H. Tang, In situ H+-mediated formation of singlet oxygen from NaBiO3 for oxidative degradation of bisphenol A without light irradiation: efficiency, kinetics, and mechanism, Chemosphere 141 (2015) 80–86.

[57] F. Nawaz, Y. Xie, J. Xiao, H. Cao, Z.A. Ghazi, Z. Guo, Y. Chen, The influence of the substituent on the phenol oxidation rate and reactive species in cubic MnO2 catalytic ozonation, Catal. Sci. Technol. 6 (2016) 7875–7884.

[58] T.X. Liu, X.Z. Li, F.B. Li, AgNO3-induced photocatalytic degradation of odorous methyl mercaptan in gaseous phase: mechanism of chemisorption and photocatalytic reaction, Environ. Sci. Technol. 42 (2008) 4540–4545.

[59] S.A. Park, H. Lim, Y.T. Kim, Enhanced oxygen reduction reaction activity due to electronic effects between Ag and Mn3O4 in alkaline media, ACS Catal. 5 (2015) 3995–4002.